



# Spark plasma sintering of Ti–1Al–8V–5Fe alloy: densification mechanism and grain growth

Wenjie Li<sup>1</sup> · Fanhao Zeng<sup>1</sup> · Lei Li<sup>1</sup> · Ziwei Wang<sup>1</sup> · Honghao Liu<sup>1</sup> · Yirui Peng<sup>1</sup> · Yi Gu<sup>2</sup>

Received: 20 May 2020 / Accepted: 11 August 2020 / Published online: 17 August 2020  
© Springer-Verlag GmbH Germany, part of Springer Nature 2020

## Abstract

The Ti–1Al–8V–5Fe (Ti185) alloys were prepared by spark plasma sintering (SPS) from TiH<sub>2</sub>, FeV, Al and Fe powders. The densification mechanism and grain-growth behavior of as-sintered alloys during SPS were investigated at temperatures of 800–1200 °C. A modified creep model considering liquid phase is proposed to modify the deviation of effective stress. The result shows that liquid phase caused by low-melting-point elemental powder can increase the effective stress, which enhances the particle rearrangement and densification. Densification stage at low temperature (800–1000 °C) without obvious grain growth and grain growth stage at 1100–1200 °C were identified during SPS process. At early densification stage, it is controlled by diffusion-controlled grain boundary sliding where the stress exponent  $n$  is close to 1, while at next stage, it is dominated by dislocation-climbing corresponding to the  $n$  close to 3. The grain-growth mechanism of SPS Ti185 during grain-growth stage was under the control of bulk and grain boundary diffusion.

**Keywords** Spark plasma sintering · Ti–1Al–8V–5Fe alloy · Densification mechanism · Grain growth

## 1 Introduction

Ti–1Al–8V–5Fe (Ti185) alloy is a metastable  $\beta$  titanium alloy, which has potential application as aerospace fastener and automotive spring due to its high ultimate strength (> 1500 MPa, room temperature), high shear strength (> 800 MPa, room temperature) and low density (about 4.6–4.7 g/cm<sup>3</sup>) [1–3]. Despite these advantages, the production of Ti185 alloy in bulk by conventional ingot processing remains a challenge. When addition of Fe in excess of 2.5 wt% in titanium alloys, it will lead to segregation of Fe, which results in the formation of inhomogeneous  $\beta$  structures ( $\beta$  flecks). These  $\beta$  flecks are detrimental to the mechanical performance of the Ti185 alloy. To reduce the Fe elemental segregation, the thermal deformation processing and heat treatment are indispensably used in the as-cast Ti185 alloy [4]. Therefore, the cost of the Ti185 alloy is very

high and approximately fifty times as much as steel, which limits its development in the market [5].

To reduce the cost of Ti185 alloy, powder metallurgy (P/M) technologies are developed to compact the titanium alloy. Among the PM technologies, blended elemental powder metallurgy (BEPM), in which alloying elements are added to titanium as elemental or master alloy powders, is one of the most promising to produce low-cost titanium parts. In addition, BEPM is quite versatile, in terms of microstructural design through alloying and sintering, and could minimize the need for machining [1, 2, 6–9]. For example, Joshi [2] prepared Ti185 alloy billet by cold isostatic pressing (CIP) and pressure-less sintering with raw material powder of TiH<sub>2</sub> and 1Al–8V–5Fe. Hamid Azizi [6] manufactured Ti185 alloy with compact structure by selective laser melting of Ti, Fe and Al–V powder. Gao et al. [7–9] fabricated Ti185 alloy with low-cost FeV<sub>80</sub> powder as raw material.

However, it also requires high sintering temperatures and long soaking times for Ti185 alloy by traditional powder metallurgy route, which usually produced coarse grains. Thus, it is vital for further thermomechanical processing and heat treatment to refine grain and improve its strength [1, 2]. Therefore, more efficient PM sintering techniques,

✉ Fanhao Zeng  
zengfanhao608@csu.edu.cn

<sup>1</sup> National Key Laboratory of Science and Technology for National Defence on High-Strength Structural Materials, Central South University, Changsha 410083, China

<sup>2</sup> College of Materials Science and Engineering, Central South University, Changsha 410083, China

such as spark plasma sintering (SPS), which can obtain fine grains in microstructure, have been proposed.

Spark plasma sintering is a novel, emerging and advanced powder consolidation method which can provide simultaneously application of axial pressure and direct current passes acting as the heating source by the Joule effect [10]. Due to the presence of plasma between powder particles, the powder surface can be activated and sintered to outstanding properties and limited grain growth at low temperature and short heating time. Over the past several years, SPS technique has been demonstrated to be an effective route to consolidate titanium alloys, and other materials [11–16]. However, there are few reports on the preparation of Ti185 alloy by SPS. Furthermore, a deep understanding of the densification mechanism is helpful in establishing relevant techniques and performing quality control on the final sintered products.

The densification mechanisms of SPS pure metal or ceramics are considered to be very important and have been investigated using the creep deformation model proposed by Bernard-Granger [17–19]. But the densification models of SPS considering complex alloys especially addition of low-melting-point elements were rarely studied. During the SPS process, metal element melting can alter the actual pressure

of the compact. Thus, it is required to consider the effect of low-melting-point element on the densification mechanisms during SPS. In this study, the Ti185 alloys were prepared by SPS using  $\text{TiH}_2$ ,  $\text{FeV}_{80}$ , Fe and Al powder under temperature of 800–1200 °C. Using the modified creep model, the densification mechanisms and grain-growth behavior of Ti185 alloy were discussed in detail.

## 2 Experimental

### 2.1 Sample preparation and characterization

Commercially hydrogenated titanium ( $\text{TiH}_2$ ) powder with a particle size of less than 100  $\mu\text{m}$  was used as raw titanium powder.  $\text{FeV}_{80}$ , Fe and Al powders with a particle size of less than 100  $\mu\text{m}$  are blended with  $\text{TiH}_2$  under the protection of argon according 86Ti:1Al:8V:5Fe (wt%) ratio to obtain Ti185 green powders.

The schematic diagram of preparation of Ti185 alloy by SPS is shown in Fig. 1a. In brief, the green powders were placed in a graphite mould with a 20 mm internal diameter which had been lined with thick graphitic sheet previously. Subsequently, the graphite mould was put into the SPS

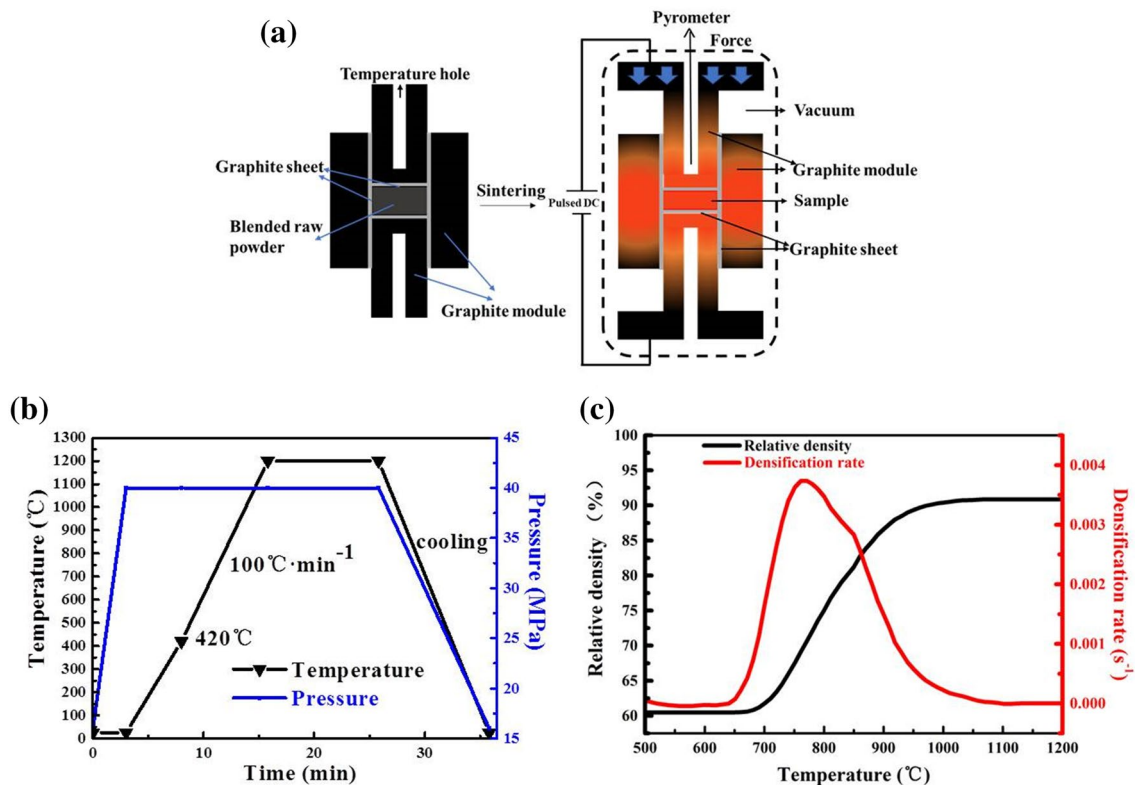


**Fig. 1** a The schematic diagram for preparation Ti185 alloy by spark plasma sintering; b typical sintering curve of the samples by spark plasma sintering; c densification rate and relative density as functions

of temperature for the Ti185. The heating rate was fixed at 100 °C  $\cdot$  min $^{-1}$  and the applied pressure is 40 MPa

chamber (HP D25/3, FCT Germany). The green powders were then pre-pressed under an axial force of 5 kN, and increased to pressure of 40 MPa. All samples were sintered at temperature of 800–1200 °C for 20–30 min with heating rate of 100 °C·min<sup>-1</sup> under fixed pressure of 40 MPa. After sintering, the furnace was cooled to room temperature by water cooling. A typical sintering program is illustrated in Fig. 1b.

After the SPS experiment, the Ti185 specimens were ground, then polished for characterization. The densities of the sintered specimens were measured using Archimedes methods, and the theoretical density was calculated by the rule of mixtures as 4.65 g/cm<sup>3</sup>. The microstructure of the Ti185 alloys was characterized by metallographic microscope (MeF3A) after standard metallographical practice and etching in Kroll's reagent for 15–60 s (100 ml H<sub>2</sub>O, 5 ml HNO<sub>3</sub> and 3 ml of 3% HF). The average grain size was measured from the optical images, which considered at least twenty images of each sample. The crystalline structure was carried out using X-ray diffractometry (XRD, D/max2550, Rigaku) with Cu–K $\alpha$  radiation. Samples for transmission electron microscopy (TEM, FEI Tecnai F20) analysis were prepared by conventional mechanical grinding and polishing until 50 nm. Holes were introduced by twin-jet electrolytic polishing, and thin-film areas around these holes were examined. Electrolytic polishing was conducted with a mixture of sulfuric acid and methanol (H<sub>2</sub>SO<sub>4</sub>/CH<sub>3</sub>OH = 5:95, vol pct) at – 50 °C and a voltage of 20 V.

## 2.2 Densification model of SPS

The changes in the height of the sample are determined by the displacement of the piston. To correct the displacement of the piston, pre-sintering was carried out without samples to obtain accurate change in height by subtracting the thermal expansion of the graphite module and pressing heads. The instantaneous relative density ( $D$ ) can be calculated from the sample height variation as follows:

$$D = \frac{h_f}{h} D_f \quad (1)$$

where  $h$  is the instantaneous height,  $h_f$  is the final height of sample and the  $D_f$  is the final relative density.

Matter transport during sintering with an external load can be considered as analogous to that occurring in high-temperature creep. For hot-pressing and SPS, a densification model was suggested by Bernard-Granger and Guizard based on the steady-state creep [17–19]. This creep model has been applied in several ceramic materials [20–24] and metal materials [25, 26] for understanding the densification mechanisms during SPS and HP.

According to steady-state creep model, the constituted kinetic equations can be written as:

$$\dot{\epsilon} = \frac{d\epsilon}{dt} = \frac{1}{D} \frac{dD}{dt} = A \frac{\Phi \mu_{\text{eff}} b}{kT} \left(\frac{b}{G}\right)^p \left(\frac{\sigma_{\text{eff}}}{\mu_{\text{eff}}}\right)^n \quad (2)$$

where  $\dot{\epsilon}$  is the creep rate,  $t$  the time,  $A$  a constant,  $\Phi$  the diffusion coefficient,  $b$  the Burgers vector,  $k$  the Boltzmann constant,  $T$  the absolute temperature,  $G$  the grain size,  $\mu_{\text{eff}}$  the instantaneous shear modulus of the powder bed,  $\sigma_{\text{eff}}$  the instantaneous effective stress acting on the powder bed,  $p$  the grain size exponent and  $n$  the stress exponent.

The instantaneous effective stress  $\sigma_{\text{eff}}$  can be written as [27]:

$$\sigma_{\text{eff}} = \frac{1 - D_0}{D^2(D - D_0)} \sigma_{\text{mac}} \quad (3)$$

where  $\sigma_{\text{mac}}$  the macroscopic compaction pressure applied to the powder bed, and  $D_0$  is the starting green density.

It is proposed by Lam et al. [28] that the effective Young's modulus of incomplete dense material synthesized by PM method can be described by:

$$E_{\text{eff}} = E_{\text{th}} \left(1 - \frac{P}{P_0}\right) \quad (4)$$

where  $E_{\text{th}}$  is the Young's modulus of the theoretically dense material,  $P = 1 - D$  is the fractional porosity of sintered sample and  $P_0 = 1 - D_0$  is the fractional porosity of the green body. Besides, the effective Young's modulus,  $E_{\text{eff}}$ , can be linked with effective shear modulus  $\mu_{\text{eff}}$  by following relation:

$$\mu_{\text{eff}} = \frac{E_{\text{eff}}}{2(1 + \nu_{\text{eff}})} = \frac{E_{\text{th}}}{2(1 + \nu_{\text{eff}})} \frac{D - D_0}{1 - D_0} \quad (5)$$

where  $\nu_{\text{eff}}$  is effective Poisson's ratio.

According to the relations above, the Eq. (2) can be transformed as follows:

$$\frac{1}{\mu_{\text{eff}}} \frac{1}{D} \frac{dD}{dt} = K \frac{e^{-\frac{Q_d}{RT}}}{T} \left(\frac{b}{G}\right)^p \left(\frac{\sigma_{\text{eff}}}{\mu_{\text{eff}}}\right)^n \quad (6)$$

where  $K = Ab\Phi/k$  is a constant,  $t$  the time,  $Q_d$  the apparent activation energy of the mechanism controlling densification,  $R$  the gas constant,  $T$  the absolute temperature.

## 3 Results

As mentioned above,  $E_{\text{th}}$  is the key parameter for calculating  $\mu_{\text{eff}}$ . In general, the Young's modulus of Ti–10V–2Fe–3Al alloy [29] and Ti–6Al–4V [30] alloy is 120 GPa and 65–153 GPa, respectively. The Poisson's

ratio of Ti–6Al–4V is 0.33 [30]. Considering that the main matrix in the sintering process is titanium, we selected key parameter of titanium ( $E_{th} = 115$  GPa,  $\nu_{eff} = 0.33$ ) for calculation. The  $D_0$  calculated by Eq. (1) is about 60% when an applied stress of 40 MPa was reached. The symbols used in this manuscript are listed in Table 1.

Figure 1c presents the variations of the relative density and densification rate ( $\frac{1}{D} \frac{dD}{dt}$ ) as functions of temperature. It appears that a clear peak of the densification rate exists centered around 750 °C and a short plateau between 700 and 850 °C, showing a significant densification of the Ti185 powders in this temperature range. Correspondingly, the temperature range of 800–1000 °C was chosen for the densification kinetics.

During the sintering process, aluminum will become a liquid phase before it is diffused into titanium crystal lattice. When the Al melted, the axial pressure applied to the graphite die forced the powders to fill up the vacancies and improved their contacts with the other powders, then the formed liquid Al filled the connected pores within the matrix (Fig. 2a). Assuming that the solid particles are identical spheres, the effective density,  $D_{real}$ , can be described as:

$$D_{real} = \frac{h_f - \frac{m_0 C}{\rho_{th} \pi r^2}}{h - \frac{m_0 C}{\rho_{th} \pi r^2}} D_f \quad (7)$$

where  $m_0$  is the mass of the powder,  $C$  is the volume ration of the Al,  $r$  is the radius of the die.  $\rho_{th}$  is the theoretical density of Ti185 alloy. Compared to Eq. (1), the influence of formed liquid phase on relative density was considered in this case.

The geometric relationship of the average area  $S$  of contact between two adjacent particles is:

$$S = \frac{\pi(D_{real} - D_0)}{3(1 - D_0)} r_0^2 \quad (8)$$

where  $r_0$  is the initial particle radius. For the compact under macroscopic applied pressure  $\sigma_{mac}$ , the average contact force,  $f$ , is expressed as follows:

$$f = \frac{4\pi r_0^2}{ZD_{real}} \sigma_{mac} \quad (9)$$

where  $Z = 12 D_{real}$  is the contact neighbors per particle [27]. It is assumed that the pressure transfer mainly relies on solid contact particles at lower relative density stage. The contact force produces a contact pressure, which corresponds to the effective applied pressure,  $\sigma_{eff}$ , on each particle contact, then shown as follows:

$$\sigma_{eff} = \frac{f}{S} = \frac{1 - D_0}{D_{real}^2 (D_{real} - D_0)} \sigma_{mac} \quad (10)$$

In Bernard-Granger's original model, effective applied pressure was calculated by apparent relative density. For the calculation of liquid phase existence in this experiment, the  $D_{real}$  can be used to obtain the effective stress more accurately. This is proven by Fig. 2b–d, which show the comparison of  $\sigma_{eff}$  obtained by the original model and by the liquid-phase model. It shows that the deviation of effective apparent pressure calculated by Eqs. (3) and (10) obviously decreased with the increase of the relative density. The liquid phase can increase the effective stress  $\sigma_{eff}$ , but the deviation is small due to the small amount of Al. With the temperature increase, the effective stress  $\sigma_{eff}$  decreases significantly with almost no deviation between two models. This is due to higher temperature, the relative density of the sample is larger, and for the same  $D_0$ , the value of  $D_{real} - D_0$  is larger, leading to the effective stress is smaller according to Eq. (10).

**Table 1** Parameters used in calculating densification mechanism

| Sign           | Parameter (unit)                     | Value    | sign        | Parameter (unit)                         | Value |
|----------------|--------------------------------------|----------|-------------|--|-------|
| $D$            | Relative density (%)                 | –        | $h_f$       | Final height (cm)                        | –     |
| $h$            | Instantaneous height (cm)            | –        | $D_f$       | Final relative density (%)               | –     |
| $D_0$          | Starting green density               | 60%      | $b$         | Burgers vector                           | –     |
| $R$            | Gas constant (J/(mol·K))             | 8.314    | $k$         | Boltzmann constant ( $10^{-23}$ J/K)     | 1.38  |
| $T$            | Temperature (°C)                     | 800–1200 | $G$         | Grain size (μm)                          | –     |
| $P$            | Grain size exponent                  | –        | $N$         | Stress exponent                          | –     |
| $\mu_{eff}$    | Instantaneous shear modulus (MPa)    | –        | $E_{th}$    | Young's modulus (GPa)                    | 115   |
| $\sigma_{eff}$ | Instantaneous effective stress (MPa) | –        | $\nu_{eff}$ | Effective Poisson's ratio                | 0.33  |
| $\sigma_{mac}$ | Macroscopic pressure (MPa)           | 40       | $Q_d$       | Apparent activation energy (kJ/mol)      | –     |
| $D_{real}$     | Effective relative density (%)       | –        | $m_0$       | Mass of raw powder (g)                   | 10    |
| $C$            | Volume ration of the Al (%)          | 1.37     | $\rho_{th}$ | Theoretical density (g/cm <sup>3</sup> ) | 4.65  |
| $r$            | Radius of the die (cm)               | 1        | $m$         | Grain-growth exponent                    | –     |



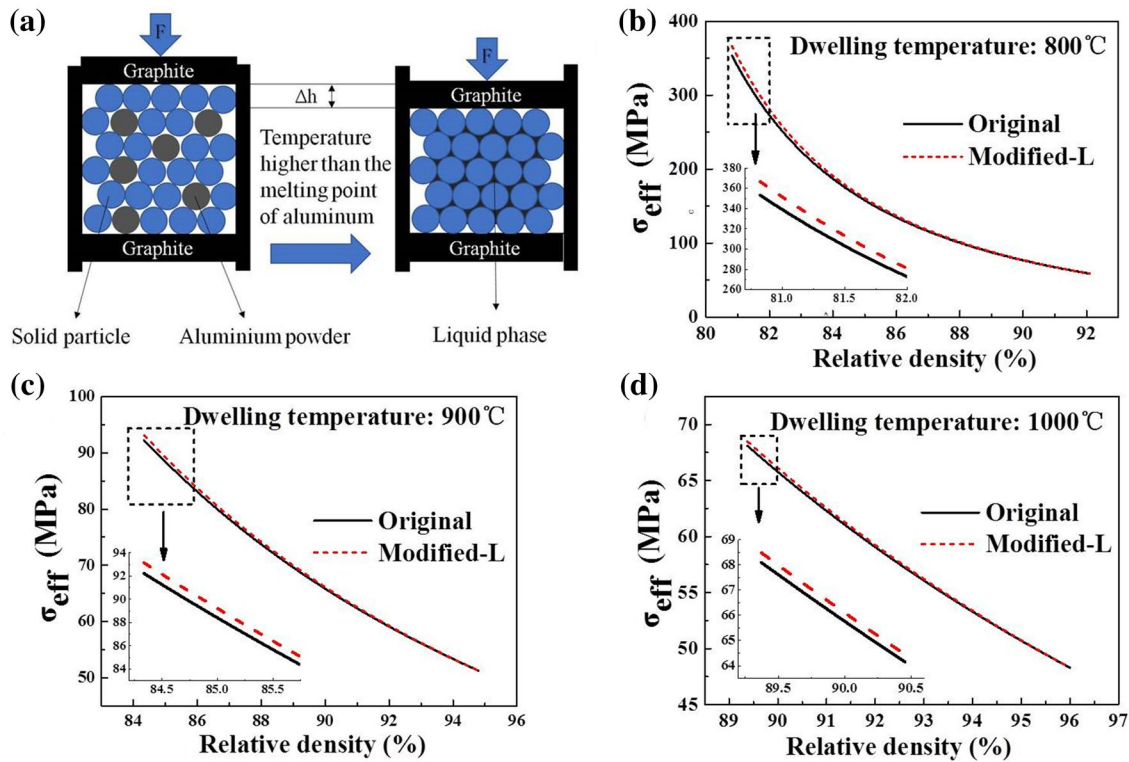


**Fig. 2** a Schematic diagram of formation process of liquid phase and process of dehydrogenation; b–d Deviation of  $\sigma_{eff}$  at dwell stage of 800–1000 °C (Modified-L is the modified effective stress considering the liquid phase)

Figure 3a shows the densification curves obtained by SPS at different temperatures when the soak time is fixed at 20 min. The relative density of all the curves increased quickly with sintering time and then reached a sluggish rate period. The higher the temperature, the higher the relative density  $D$ , whatever the soak time. It

is worth mentioning that as the sintering temperature is over 900 °C, the relative density is more than 95%. This showed the great cost reduction advantage of SPS: the sintering temperature is reduced by more than 150 °C and sintering time reduced by two-thirds compared with the traditional PM technologies.

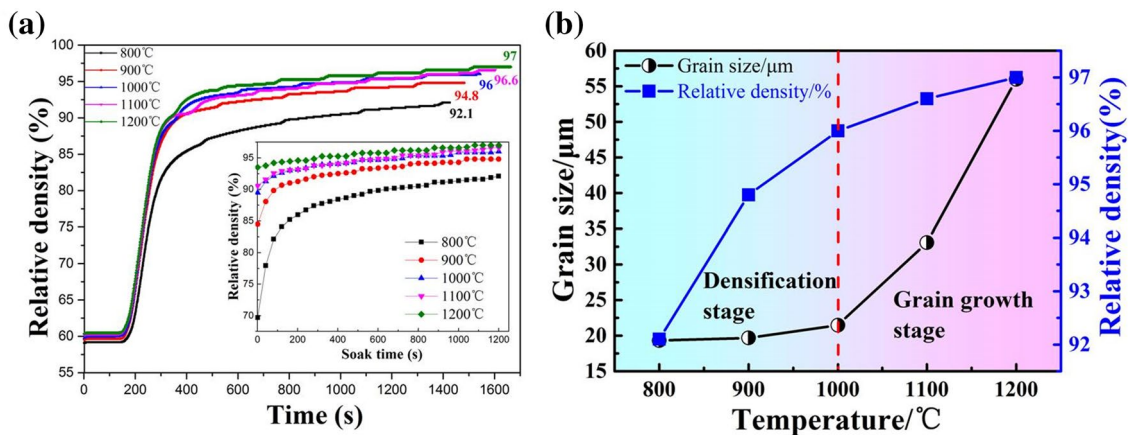


**Fig. 3** a Continuous densification curves of Ti185 samples obtained by SPS at different temperatures under pressure of 40 MPa. Inset: the densification curves of different temperature when the soak tempera-

ture is reached and for a soak time of 20 min; b Evolution of grain size and relative density of Ti185 at different sintering temperatures ( $t=30$  min,  $P=40$  MPa)

Figure 3b presents the grain size and relative density evolutions as functions of temperature. Clearly, based on the evolution of grain growth, the sintering process can be divided into two stages; at the densification stage (800–1000 °C), the relative density increases quickly from 92.1 to 96% without apparent grain growth. Nevertheless, the grain size grows rapidly from about 20 to 55  $\mu\text{m}$  as the temperature increases to 1200 °C. The microstructures of Ti185 samples for different temperatures are provided in Fig. 4. Equiaxed grain was generally observed and the original powder shape disappeared, indicating transformed to the later stage of densification with high relative density. In

addition, the residual porosity was found to be dependent on the sintering temperature. At temperatures of 800–1000 °C, a few closed and spherical pores are observed. Unlike lower temperatures, few pores exist in higher temperatures (1100, 1200 °C). What is more, grain size grows nonlinearly during 1100–1200 °C (Fig. 3b), more coarse grains ( $G \geq 55 \mu\text{m}$ ) are observed at 1200 °C when the final relative density  $D$  reaches 98%. Compared with the traditional melting casting and CIP P/M sintering [8, 9], the grains of SPS are significantly smaller.

Figure 5 shows typical XRD pattern and TEM pictures of Ti185 sample sintered at 1000 °C. The major phase of

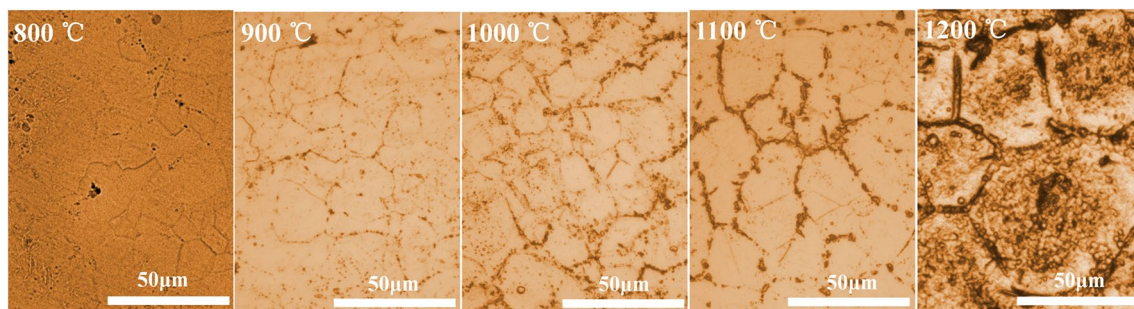


Fig. 4 Typical microstructure of the Ti185 samples sintered at 800–1200 °C ( $t = 30 \text{ min}$ ,  $P = 40 \text{ MPa}$ )

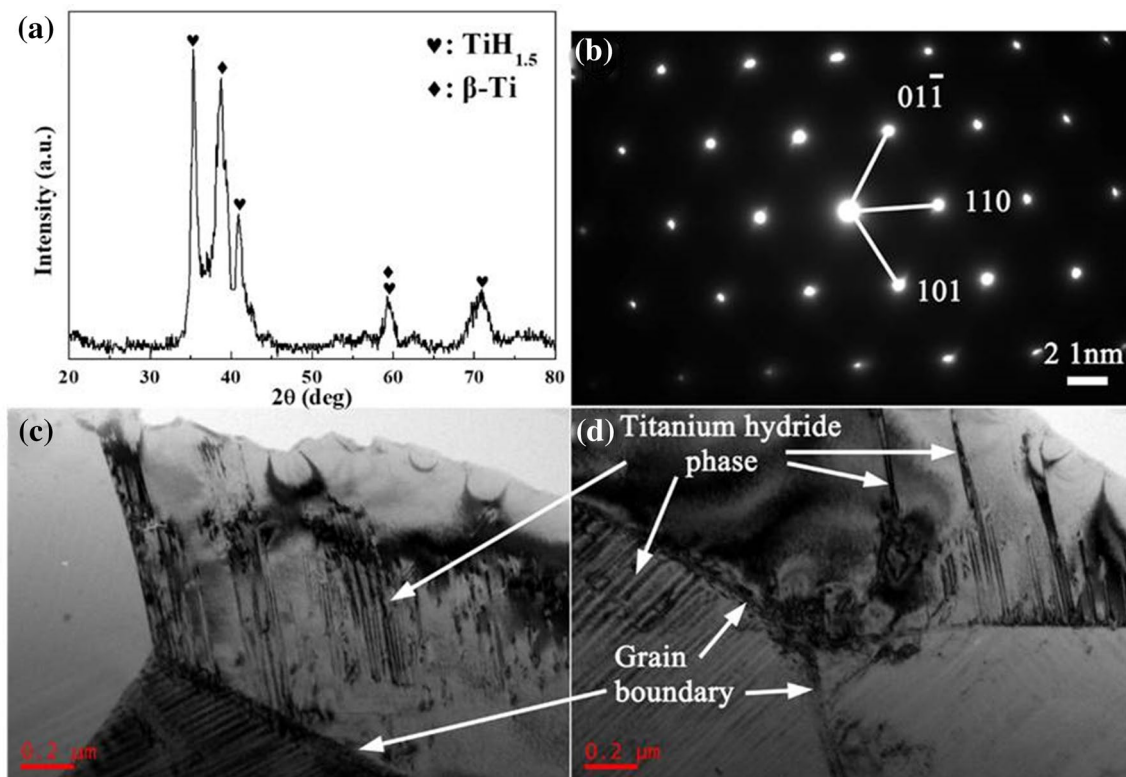


Fig. 5 Representative X-ray diffraction pattern (a) and TEM images (b–d) along  $[111]_{\beta}$  axis of Ti185 sample sintered by SPS at 1000 °C for 30 min

sample is  $\beta$ -Ti, which is more suitable for hot-working compared to other structure, such as bimodal and basketweave structures. Some titanium hydride ( $\text{TiH}_{1.5}$ ) can be identified for non-completely dehydrogenated during sintering (Fig. 5a). As the connection between the particles becomes dense, the hydrogen atoms need to diffuse through the outer Ti layer to escape, and the dehydrogenation rate of titanium hydride will reduce, leading to some residual hydrogen in the sample. From the TEM pictures obtained along  $[111]_{\beta}$  axis (Fig. 5b–d), we noticed the lamellar titanium hydride ( $\text{TiH}_{1.5}$ ) with submicron widths and several microns long clearly. The lamellar  $\text{TiH}_{1.5}$ , may be, is undesirable with respect to mechanical properties, particularly fatigue performance, but it can be removed or deformed by subsequently heat treatment and hot-working.

### 4 Discussion

#### 4.1 Densification mechanism

To make a suggestion concerning the densification mechanism of the blend raw powder during SPS, it is critical to evaluate the key densification parameters  $n$ ,  $p$  and  $Q_d$  in relation (6). Hence, grain size may be assumed to be constant when the temperature is in the range 800–1000 °C (Fig. 3b). In this case, the value of  $p$  should be left out in consideration of that  $(b/G)$  is a constant. Here, the  $n$  can be more easily calculated assuming  $Q_d$  is a constant value at the temperature range. In this case, the relation (6) can be transformed to:

$$\ln\left(\frac{1}{\mu_{\text{eff}}}\frac{1}{D}\frac{dD}{dt}\right) = n\ln\left(\frac{\sigma_{\text{eff}}}{\mu_{\text{eff}}}\right) + K_1 \tag{11}$$

where  $K_1$  is a constant for a fixed sintering temperature. Then, the slopes of the different straight lines can be

obtained by drawing the Eq. (11) and it corresponds to the  $n$  values of different temperatures.

Figure 6a shows the variation of  $\ln\left(\frac{1}{\mu_{\text{eff}}}\frac{1}{D}\frac{dD}{dt}\right)$  in function of  $\ln\left(\frac{\sigma_{\text{eff}}}{\mu_{\text{eff}}}\right)$  for different soak temperatures. It is obvious that  $n$  exhibits different values, which represent different stress levels act on the powder compact. For the low effective compaction stress,  $n$  is about 1, the curve corresponds to the early stage of dwelling at 800–1000 °C. At the later stage of dwelling at 800–1000 °C, the stress exponent of  $n$  shows a high value which is close to 3. At this point, it appears that different mechanisms may be invoked for the control of densification during SPS of the Ti185 blend powder selected. The  $n$  values turn to 4.4 and 6.36 when the dwelling temperatures are 1100 °C and 1200 °C.

With the  $n$  value established, the relation (6) can be transformed as follows to evaluate  $Q_d$ , assuming a constant value for  $n$  and  $p$  for a given value of the activation energy:

$$\ln\left(\frac{T}{\mu_{\text{eff}}}\left(\frac{\mu_{\text{eff}}}{\sigma_{\text{eff}}}\right)^n\frac{1}{D}\frac{dD}{dt}\right) = -\frac{Q_d}{RT} + K_2 \tag{12}$$

where  $K_2$  is a constant. The slope of the straight line obtained when drawing  $\ln\left(\frac{T}{\mu_{\text{eff}}}\left(\frac{\mu_{\text{eff}}}{\sigma_{\text{eff}}}\right)^n\frac{1}{D}\frac{dD}{dt}\right) = -f\left(\frac{1}{T}\right)$  corresponds to the value of  $-Q_d/R$ . From relation (12), the values of  $D$  need to be determined first, and the function  $\frac{1}{D}\frac{dD}{dt}$  should be determined.

Figure 6b draws the variation of  $\frac{1}{D}\frac{dD}{dt}$  as a function of relative density  $D$ . To calculate  $Q_d$ , two values of  $\frac{1}{D}\frac{dD}{dt}$  have then been chosen at different stages:  $0.003\text{ s}^{-1}$  corresponding to low effective compaction stress exponent ( $n = 1$ );  $0.0005\text{ s}^{-1}$  corresponding to high-effective compaction stress exponent ( $n = 3$ ).

By now, the corresponding relative density values can be obtained, which enables the calculation of the corresponding values of  $\sigma_{\text{eff}}$  and  $\mu_{\text{eff}}$ . Hence, the value of  $\ln\left(\frac{T}{\mu_{\text{eff}}}\left(\frac{\mu_{\text{eff}}}{\sigma_{\text{eff}}}\right)^n\frac{1}{D}\frac{dD}{dt}\right)$

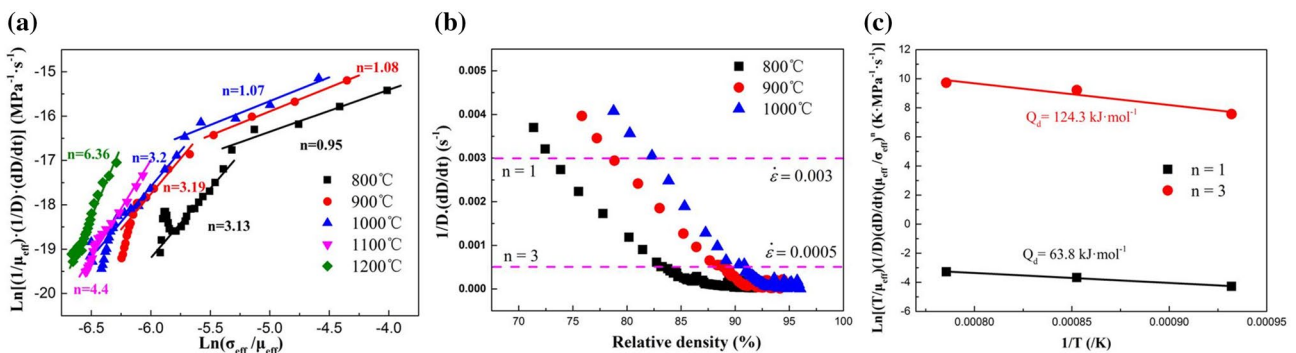


**Fig. 6** a Effective stress exponents calculated with Eq. (11) for different SPS temperatures. The stress exponent values are the slopes of the straight lines; b the curves of different sintering temperature to determine the values of  $\frac{1}{D}\frac{dD}{dt}$  and the corresponding relative density values

when  $n$  is 1 or 3; c Apparent activation energy for densification,  $Q_d$ , when effective stress exponent  $n$  is 1 and 3. The slope of the straight lines is  $-Q_d/R$



as a function of  $1/T$  can be drawn, as shown in Fig. 6c. According to Eq. (12), the slope of the fitting line corresponds to the value  $-Q_d/R$ ; thus, two values of  $Q_d$  can be calculated:  $Q_d = 63.8 \text{ kJ}\cdot\text{mol}^{-1}$  when  $n = 1$ ;  $Q_d = 124.3 \text{ kJ}\cdot\text{mol}^{-1}$  when  $n = 3$ .

For Ti–Al–V–Fe alloy, Yang [31] studied the solid-state sintering behavior of Ti–10V–2Fe–3Al (Ti 1023) by P/M technique and determined that their apparent activation energy  $Q_d$  was  $163 \pm 13 \text{ kJ}\cdot\text{mol}^{-1}$ , while Panigrahi [32] reported as  $184 \text{ kJ}\cdot\text{mol}^{-1}$ . To eliminate the deviation by the stress exponent  $n$ , Antou [33] used different pressures to calculate  $Q_d$ . It is reported [34] that fine-grained Ti produced by SPS has the activation energy of  $115 \text{ kJ}\cdot\text{mol}^{-1}$  under the pressure of 80 MPa. In our present work, a fixed pressure of 40 MPa was applied and the  $Q_d$  is  $63.8 \text{ kJ}\cdot\text{mol}^{-1}$  and  $124.3 \text{ kJ}\cdot\text{mol}^{-1}$ , lower than that of traditional P/M.

The effective stress exponent,  $n$ , is an important parameter involved in controlling the densification mechanism of SPS. Usually, different  $n$  values correspond to different densification mechanisms. Through studies, the densification behavior of SPS materials, such as alumina by Santanach [23], zirconia and  $\text{MgAl}_2\text{O}_4$  by Burnard-Granger [24–26], tungsten by Deng [35], it is considered that when  $n$  is low, the densification is dominated by grain boundary sliding, which contains in-series interface-reaction/lattice diffusion. Hence, it is reasonable to determine that for the present SPS Ti185, the densification mechanism is grain boundary sliding controlled by diffusion at low stress exponents' regime.

For the liquid sintering of P/M, Kingery [36, 37] proposed a classical theory that it is composed of three densification processes: first, rearrangement of solid particles to give increased density; second, solution precipitation in which material is dissolved away from contact points, allowing the centers of particles to approach; and finally, coalescence of solid particles with a cessation of sintering. Many P/M experiments [38] conform to the theory. However, the classical theory does not take grain growth into account. Kang [39] and Lee [40], hence, proposed a Pore-Filling model. They consider that when powder is sintered in the presence of liquid phase, rapid densification and grain growth will occur even in the early stage of sintering. As the grains grow, the surfaces of the smaller pores were completely wetted to critical size, and then the liquid will spontaneously fill the pores. After a long sintering, the liquid was eliminated by microstructure homogenization. This is proven by Zhang [20], which shows high-entropy alloys (HEA) did not react with the  $\text{B}_4\text{C}$  matrix during SPS, and reduced  $Q_d$  to  $75 \text{ kJ}\cdot\text{mol}^{-1}$ , promote densification and grain growth.

Considering the densification rate reaches its maximum at  $750 \text{ }^\circ\text{C}$  slightly higher than the melting point of Al (Fig. 1c), as well as the grains grow only at higher temperatures (Fig. 3b), it is reasonable to determine that the sintering process is instantaneous liquid-phase sintering. When the

sintering temperature exceeds  $660 \text{ }^\circ\text{C}$ , the Al powder melts to form a liquid phase. Under an external force, the liquid phase flows into the pores and the solid particles slide and rearrange, which contributes significantly to the densification rate. Because the liquid of Al is an alloying element and will gradually diffuse into the Ti matrix, it is different with the classic Kingery theory. The most cases of SPS Ti185 are the diffusion of Al atoms into the crystal lattice of titanium, making the sintering process similar to the instantaneous liquid-phase sintering process.

However, for high-effective stress-value exponent,  $n$  close to 3, the densification mechanism can be understood by considering the dislocation climb theory of steady-state creep [41, 42]. The creep rate is expressed as follows:

$$\dot{\epsilon} = \frac{b}{6d^3(\pi Md)^{1/2}} V_m \quad (13)$$

where  $b$  is the Burgers vector of the edge dislocation involved in the process,  $d$  the distance between two neighboring plans emitting the involved dislocations,  $M$  the dislocation source density, and  $V_m$  the climbing rate of the involved dislocation.

When  $\sigma b^3 \ll kT$ , the dislocation-climbing rate could be expressed by:

$$V_m \propto \frac{D_V \sigma b^3}{bkT} \quad (14)$$

where  $D_V$  is the volume (lattice) diffusion coefficient of vacancies,  $\sigma$  is the applied stress.

When  $M$  is a function of applied stress, the relation may be expressed by:

$$M \propto \left( \frac{\sigma}{\mu b} \right)^3 \quad (15)$$

Thus, by combining the above equations, the final expression for climb-controlled creep mechanism is as follows:

$$\dot{\epsilon} = K_3 \frac{D_V}{b^2} \left( \frac{\sigma}{\mu} \right)^3 \frac{\mu b^3}{kT} \quad (16)$$

where  $K_3$  is a constant,  $\mu$  is the shear modulus.

In the present SPS experiment, taking into account the diffusion coefficient,  $D_V$  can be expressed as  $D_V = D_{0V} \exp(Q_V/RT)$ , where  $D_{0V}$  is a constant pre-exponential factor, the relation (16) can be transformed into:

$$\frac{1}{\mu_{\text{eff}}} \frac{1}{D} \frac{dD}{dt} = K_4 \frac{e^{-\frac{Q_V}{RT}}}{T} \left( \frac{\sigma_{\text{eff}}}{\mu_{\text{eff}}} \right)^3 \quad (17)$$

where  $K_4$  is a constant.

When the soak temperatures are  $800\text{--}1000 \text{ }^\circ\text{C}$  during our SPS experiments, the stress exponent values are very



close to 3 (Fig. 6a), which is in analogy with relations (17) derived from Weertman's [41, 42] investigations. Therefore, at the stage when  $n$  value is close to 3, the material creep mechanism is controlled by dislocation climb. TEM observation dislocation of sintered sample is shown in Fig. 7. The pictures along the  $[111]_{\beta}$  axis (Fig. 7a, c) and  $[001]_{\beta}$  axis (Fig. 7b, d) show clearly the presence of dislocations which was pointed out by the arrow. According to  $n$  value, the dominant creep mechanism during SPS may be the dislocation-climbing mechanism. However, when the sintering temperature is 1100 °C, the stress exponent calculated is  $n=4.4$ , much larger than the value of 3, which indicates that the densification mechanism controlled by dislocation climb became more stable. With higher temperature of 1200 °C, the sample has high  $n$  (6.4), then it tends to transform to grain-growth mechanism.

## 4.2 Grain growth

The creep model proposed by Bernard-Granger, can be used to calculate and analyze densification mechanism based on constant grain size. However, in the SPS Ti185, when the sintering temperature exceeds 1000 °C, the grain grows apparently. It indicates that at the low temperature, sintering and dwelling processes mainly promote powder densification. While at high soaking temperatures ( $T > 1000$  °C), due

to the high density ( $D > 96\%$ ), it will promote grain growth. Using the widely known grain growth power law [43, 44], we can describe the relation:

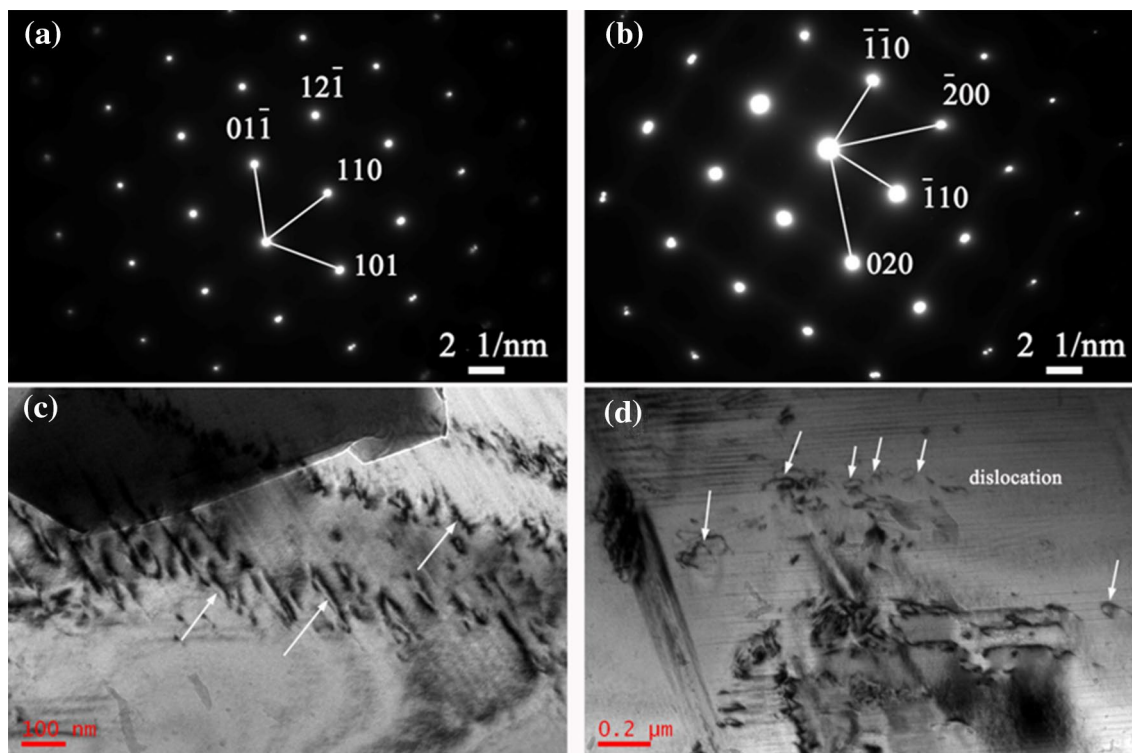
$$G_t^m - G_0^m = K_0 t \quad (18)$$

where  $G_t$  and  $G_0$  are grain sizes at time  $t$  and  $t=0$ ,  $m$  the grain-growth exponent,  $K_0$  a constant.

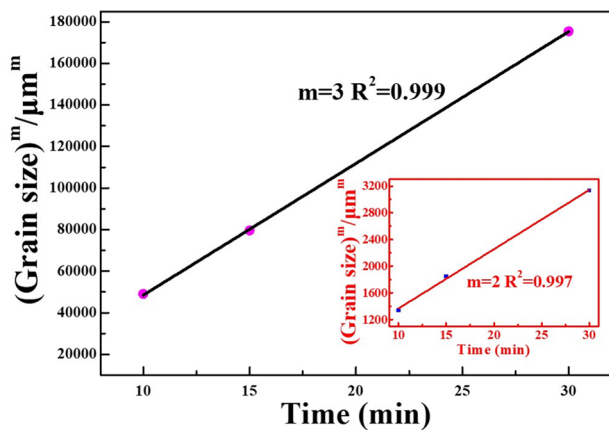
For a single-phase system, the possible value of grain-growth exponent  $m$ , which is known as the kinetic parameter, was reported to be 2 or 3. Different values of  $m$  correspond to different grain-growth mechanisms. When  $m=2$ , the main mechanism controlling grain growth is grain boundary diffusion. When  $m=3$ , grain growth is mainly controlled by the bulk diffusion or through a liquid-phase diffusion. Thus, we assumed the  $m$  to be 2 or 3 for the SPS Ti185 alloy.

Figure 8 shows the linear fittings for different values of grain-growth exponent  $m$ . By plotting the linear fitting results obtained at dwelling times 10, 15, and 30 min when the dwelling temperature is fixed at 1200 °C, we can determine the main mechanism of grain growth. According to the regression coefficients  $R^2$ , both two  $m$  values are acceptable ( $R^2=0.999$  for  $m=3$  and  $R^2=0.997$  for  $m=2$ ).

It can be noted that, no matter the value of  $m$  is 2 or 3, the results of linear fitting are in good agreement with the Eq. (18); however, when  $m=3$ , the result of linear fitting



**Fig. 7** Typical TEM images of Ti185 sample sintered at 1000 °C for 30 min by SPS: **a** and **c** along the  $[111]_{\beta}$  axis; **b** and **d** along  $[001]_{\beta}$  axis



**Fig. 8** Linear fittings for different value of grain-growth exponent  $m$  (2 and 3) obtained at 1200 °C and dwelling time 10, 15, and 30 min

is more in accordance with the Eq. (18). Hence, for higher temperature, it is reasonable to conclude that grain-growth mechanism is mainly controlled by the bulk diffusion, or liquid diffusion. The presence of a liquid phase could account for the rapid densification obtained for lower temperatures (800–1000 °C) and the grain growth of high temperature. At the same time, the calculated results showed that grain boundary diffusion also played a non-negligible role in grain growth according to the value of  $R^2$  when  $m=2$ . This result implies that the control mechanisms for grain growth include bulk diffusion and grain boundary diffusion.

In addition to this, at the sintering stage with temperature above 1000 °C, grain-growth process is a grain boundary migration related to the reaction of pores and grain boundaries. The grain boundaries migrate, which is from change of chemical potential caused by pressure difference between two sides of interface caused by curvature radius of interface, towards the tendency of energy reduction, resulting in a certain degree of grain growth in the material. At the same time, when the grain boundary displacement changes the curvature of the pore surface, there is a driving force of material migration, which makes atoms migrate between grain boundaries and pores. Grain boundaries with high energy will carry the pores along with them, promoting further densification of the alloys. The mechanism of mass transfer in nature is still evaporation and condensation, surface diffusion or volume diffusion.

## 5 Conclusion

A modified creep model considering liquid was proposed and applied to investigate the densification mechanisms of SPS Ti185 alloy at 800–1200 °C. The sintering process shows two stages: densification without grain growth occurring at

the lower temperatures of 800–1000 °C and grain-growth stage at higher temperatures (1100 °C, 1200 °C). At early densification, the effective compaction stress exponent is low ( $n=1$ ) and the apparent activation energy  $Q_d$  is calculated as 63.8 kJ·mol<sup>-1</sup>, indicating its mechanism of diffusion-controlled grain boundary sliding. For higher effective compaction stresses ( $n$  closed 3,  $Q_d=124.3$  kJ·mol<sup>-1</sup>), the densification is mainly controlled by dislocation motion. The grain growth is mainly controlled by grain boundary migration and diffusion. The liquid phase may be promoted not only for the densification of Ti 185, but also its grain growth during SPS process.

**Acknowledgements** The authors acknowledge funding from the National Key R&D Program of China (Grant No. 2017YFE0301502) and National Key Laboratory of Science and technology for National Defence on High-strength Structural Materials (No. 6142912180203, 6142912180201).

## References

1. A. Devaraj, V.V. Joshi, A. Srivastava et al., *Nat. Commun.* **7**, 11176 (2016)
2. V.V. Joshi, C. Lavender, V.S. Moxson et al., *J. Mater. Eng. Perform.* **22**, 995 (2013)
3. W. Gerhard, R.R. Boyer, E.W. Collings, *Materials Properties Handbook: Titanium Alloys* (ASM Intl, Materials Park, 1994)
4. J.G. Ferrero, *Rare. Metal. Mat. Eng.* **35**, 209 (2006)
5. F.H. Froes, M.A. Imam, *Key Eng. Mater.* **436**, 1 (2010)
6. A. Hamid, Z. Hatem, *Addit. Manuf.* **21**, 529 (2018)
7. S. Gao, P. Liu, C. Wang et al., *Powder metallurgy. Technology.* **32**, 427 (2014)
8. Y. Zhang, C. Wang, Y. Zhang et al., *Mater. Manuf. Process.* **32**, 1869 (2017)
9. Y. Zhang, Z. Zhang, S. Liu et al., *Mater. Manuf. Process.* **33**, 1830 (2018)
10. Z.A. Munir, U. Anselmi-Tamburini, M. Ohyanagi, *J. Mater. Sci.* **41**, 763 (2006)
11. N.S. Weston, F. Derguti, A. Tudball et al., *J. Mater. Sci.* **50**, 4860 (2015)
12. Y. Wang, C. Zhang, Y. Liu et al., *Mater. Charact.* **128**, 75 (2017)
13. J. Wang, Y. Wang, Y. Liu et al., *Intermetallics* **64**, 70 (2015)
14. H. Chen, F. Zeng, W. Li et al., *Ceram. Int.* **45**, 12122 (2019)
15. J. Liu, F. Zeng, Z. Zou, *J. Mater. Res.* **32**, 3425 (2017)
16. C. Yang, M.D. Zhu, *Scripta Mater.* **139**, 96 (2017)
17. G. Bernard-Granger, C. Guizard, *Acta Mater.* **55**, 3493 (2007)
18. G. Bernard-Granger, C. Guizard, *J. Mater. Res.* **24**, 179 (2009)
19. R.J. Brook, E. Gilbert, D. Hind, J.M. Vieira, in *Sintering Theory and Practice*, ed. by D. Kolar, S. Pejovnik, M.M. Ristic (Elsevier, Amsterdam, 1982), p. 585
20. M. Zhang, R. Li, T. Yuan et al., *Scripta Mater.* **163**, 34 (2019)
21. G. Bernard-Granger, A. Addad, G. Fantozzi et al., *Acta Mater.* **58**, 3390 (2010)
22. M. Gendre, A. Maître, G. Trolliard, *Acta Mater.* **58**, 2598 (2010)
23. J.G. Santanach, A. Weibel, C. Estournès et al., *Acta Mater.* **59**, 1400 (2011)
24. G. Bernard-Granger, N. Benameur, A. Addad et al., *J. Mater. Res.* **24**, 2011 (2009)
25. L. Ramond, G. Bernard-Granger, A. Addad et al., *Acta Mater.* **58**, 5120 (2010)

26. G. Bernard-Granger, N. Amandine, C. Navone et al., *J. Mater. Sci.* **47**, 4313 (2012)
27. A.S. Helle, K.E. Easterling, M.F. Ashby, *Acta Metall.* **33**, 2163 (1985)
28. D.C.C. Lam, F.F. Lange, A.G. Evans, *J. Am. Ceram. Soc.* **77**, 2113 (1994)
29. X. Ma, F. Li, J. Cao et al., *J. Alloy. Compd.* **703**, 298 (2017)
30. J. Dong, F. Li, C. Wang, *Mater. Sci. Eng. A.* **580**, 105 (2013)
31. Y.F. Yang, S.D. Luo, G.B. Schaffer et al., *Mater. Sci. Eng. A.* **528**, 6719 (2011)
32. B.B. Panigrahi, M.M. Godkhindi, K. Das et al., *Mater. Sci. Eng. A.* **396**, 255 (2005)
33. G. Antou, P. Guyot, N. Pradeilles et al., *J. Mater. Sci.* **50**, 2327 (2015)
34. J. Kozlík, H. Becker, J. Stráský et al., *Mater. Sci. Eng. A* **772**, 138783 (2020)
35. S. Deng, T. Yuan, R. Li et al., *Powder. Technol.* **310**, 264 (2017)
36. W.D. Kingery, *J. Appl. Phys.* **30**, 301 (1959)
37. W.D. Kingery, M.D. Narasimhan, *J. Appl. Phys.* **30**, 307 (1959)
38. E. Carnall, *Mater. Res. Bull.* **2**, 1075 (1967)
39. S.J.L. Kang, K.H. Kim, D.N. Yoon, *J. Am. Ceram. Soc.* **74**, 425 (1991)
40. S.M. Lee, S.J.L. Kang, *Acta Mater.* **46**, 3191 (1998)
41. J. Weertman, *Trans. Am. Soc. Met.* **61**, 681 (1968)
42. J. Weertman, *J. Appl. Phys.* **28**, 362 (1957)
43. R. Chaim, A. Shlayer, C. Estournes, *J. Eur. Ceram. Soc.* **29**, 91 (2009)
44. K.B. Alexander, P.F. Becher, S.B. Waters et al., *J. Am. Ceram. Soc.* **77**, 939 (1994)

**Publisher's Note** Springer Nature remains neutral with regard to jurisdictional claims in published maps and institutional affiliations.